$FeCr_2O_4$ spinel to near megabar pressures: Orbital moment collapse and site-inversion facilitated spin crossover

W. M. Xu,[1,*] G. R. Hearne,[2] S. Layek,[1] D. Levy,[1] J.-P. Itié,[3] M. P. Pasternak,[1] G. Kh. Rozenberg,[1] and E. Greenberg[1,4]

[1]*School of Physics and Astronomy, Tel Aviv University, 69978 Tel Aviv, Israel*

[2]*Department of Physics, University of Johannesburg, P.O. Box 524, Auckland Park, 2006, Johannesburg, South Africa*

[3]*Synchrotron SOLEIL, L'Orme des Merisiers, Saint-Aubin, BP 48, 91192 Gif-sur-Yvette Cedex, France*

[4]*Center for Advanced Radiation Sources, University of Chicago, Argonne, Illinois 60439, USA*

(Received 17 October 2016; revised manuscript received 11 December 2016; published 6 January 2017)

The interplay between lattice, orbital, and spin degrees of freedom in iron chromite (spinel $[Fe]\{Cr_2\}O_4$) has been investigated to near megabar pressures. The cubic-to-tetragonal transition, from static Jahn-Teller distortions at the Fe locality, rises from $T_{\text{J-T}} \sim 135$ K at ambient pressure to 300 K by ∼12 GPa. The tetragonal distortion progressively increases and orbital moment quenching is triggered beyond ∼24 GPa, as monitored by the magnetic hyperfine field H_{hf} at Fe sites. In the range 30–60 GPa, original Fe^{2+} tetrahedral sites with an unquenched orbital moment ($H_{hf} \sim 20$ T) coexist with newly evolved Fe^{2+} at tetrahedral sites having the orbital moment quenched and a resultant large $H_{hf} \sim 35$ T. Additionally, new Fe^{2+} sites having distinguishable orbital moment quenching signatures ($H_{hf} \sim 42$ T) are discerned. Those sites also have other Fe nuclear hyperfine interaction parameter values typical of Fe^{2+} in octahedral coordination. There is a concurrent change to a steeper decrease of unit-cell volume as pressure rises above ∼30 GPa. These electronic and lattice responses are interpreted as signatures of progressive partial spinel inversion from high-spin Fe ↔ Cr tetrahedral/octahedral site exchange, triggered near ∼30 GPa. Beyond 60 GPa a new diamagnetic low-spin Mössbauer spectral component emerges. This is preceded by an inflection and discontinuity in the pressure dependence of the resistance and tetragonal unit-cell volume, respectively. By ∼93 GPa, half of the iron is low spin in octahedral sites from evolved tetragonal-spinel inversion processes. The remainder reside in tetrahedral high-spin sites with $H_{hf} \sim 30$ T. The charge gap from electron correlations does not close, despite an anticipated appreciable band broadening from a ∼30% unit-cell volume reduction upon pressurization to ∼93 GPa. This is attributable to an increase in effective on-site repulsion (Hubbard U_{eff}) with increasing pressure or at spin crossover, specific to the $Cr^{3+}(d^3)$ and $Fe^{2+}(d^6)$ electronic configurations, respectively. Thus a ∼200 meV "Mott" gap prevails in the mixed spin-state of the partially inverted tetragonal phase $[Fe_{1-x}Cr_x]\{Fe_xCr_{2-x}\}O_4$ ($x \sim 0.5$) up to near a megabar (100 GPa) densification.

DOI: 10.1103/PhysRevB.95.045110

I. INTRODUCTION

Iron chromite $FeCr_2O_4$ has a normal spinel structure of $[A]\{B_2\}O_4$ at room temperature (RT; space group $Fd\bar{3}m$). The tetrahedrally coordinated A site is occupied by an Fe^{2+} ion, which is in the high-spin $(e)^3(t_2)^3$ configuration with $3d$ electron spin depiction $(\uparrow\uparrow\downarrow)(\uparrow\uparrow\uparrow)$ corresponding to atomic spin $S = 2$. Thus, an electron with the minority spin ($\downarrow$) in the low lying e orbitals has an orbital degree of freedom and, as such, renders this a Jahn-Teller (J-T) active ion. The octahedrally coordinated B site is occupied by the Cr^{3+} ion, which involves the $(t_{2g})^3$ electronic configuration without an orbital degree of freedom. The Cr cations form the nodes of a geometrically spin frustrated pyrochlore sublattice, so interesting magnetic properties may be anticipated.

The compound has a rather rich magnetic phase diagram in that collinear ferrimagnetic order occurs below ∼80 K, followed by conical spiral magnetic order below ∼35 K [1,2], or an even more complicated spin structure [3]. The spin order at both magnetic transitions has been shown to couple to infrared active phonon modes [4]. This spin-lattice coupling results in a symmetry-lowering orthorhombic distortion at the onset of magnetic order. Furthermore, a ferroelectric polarization has been measured in both ferrimagnetic and spiral magnetic states [5,6]. Thus, chromite forms part of a class of recent generation spin-driven ferroelectrics (type-II multiferroics [7]), including Fe_2TiO_4 and FeV_2O_4.

The system has also garnered recent interest because of the observation of an orbital-ordering manifestation of the cooperative J-T effect below the cubic-to-tetragonal transition at $T_{\text{J-T}} \sim 135$ K [8]. Above $T_{\text{J-T}}$ Fe Mössbauer-effect spectroscopy (MS) nicely demonstrates that a dynamical J-T effect is operative. The x-ray diffraction (XRD) data shows the system to be cubic, yet Fe MS shows conspicuous deviations from cubic-symmetry by way of doublet quadrupole splitting (QS) signatures [3,9]. This is indicative of J-T distortions reorienting dynamically among the three crystallographic axes, on a time scale comparable to the "shutter speed" of the MS quadrupole interaction probe. This time window is given by the inverse of the quadrupole precession frequency ($2\pi/\omega_Q \sim 40$ ns) [9,10].

These spinels also occur in many geological settings of the Earth's crust and mantle, as well as in lunar rocks and meteorites. The study of their high pressure structural and magnetic-electronic properties is of additional importance for improving the understanding of physical properties, dynamics, and differentiation of planetary interiors [11,12]. For example, primarily XRD pressure studies at RT have shown that related spinels undergo a transition to the tetragonal structure and then to orthorhombic postspinel structures at higher pressure

---

[*]Author to whom all correspondence should be addressed: xuw@post.tau.ac.il

[13–15]. Such postspinel polymorphs of chromite have been identified in the shock veins of the Suizhou meteorite [16]. Little is known about the magnetic-electronic aspects of these high pressure phases.

More recent structural pressure studies of spinels have focused on nanophase materials (for example, $ZnFe_2O_4$ and $CoFe_2O_4$) for comparison with the pressure response of bulk analogs [17,18]. The further physical characterization of such nanophases at extreme conditions potentially represents a new and interesting avenue of research.

Our focus in this work was to evolve specifically iron chromite through various structural and magnetic-electronic phases, upon pressurization to very high pressures of nearly a megabar in a diamond anvil cell (DAC). We have then ascertained the effect of high pressures on the interplay between the various lattice, orbital, and spin degrees of freedom. This has been accomplished by a combination of ^{57}Fe MS as a *direct probe* of the pertinent A-site J-T cation and electrical-transport measurements both at variable cryogenic temperatures, as well as synchrotron XRD structural studies at RT.

II. EXPERIMENTAL

$FeCr_2O_4$ was synthesized by a solid-state reaction using the required stoichiometric quantities of Fe, Fe_2O_3, and Cr_2O_3 at 1200 °C in a nitrogen atmosphere for 24 h. The Fe_2O_3 precursor material was enriched to ~20% ^{57}Fe. The cubic structure and magnetic properties were compatible with previous reports of phase pure samples at ambient pressure [19,20], as confirmed by conventional powder XRD and variable cryogenic temperature MS in our laboratory.

The Fe Mössbauer-effect studies were carried out using a ^{57}Co(Rh) 10-mCi point source in the 5–300 K temperature range, involving a top-loading liquid-helium cryostat [21]. The typical collection time of a spectrum was ~24 h. Spectra were analyzed using appropriate fitting programs from which the hyperfine interaction parameters and the corresponding relative abundances of the spectral components were derived [22]. The isomer shift (IS) in the present paper is calibrated relative to an α-Fe foil at ambient conditions. The Tel Aviv University (TAU) miniature piston-cylinder DAC [23], was used with anvils having 300 μm diameter culets for pressures to ~60 GPa and 200 μm diameter culets for $P > 60$ GPa. Samples were loaded into 100–150 μm diameter cavities drilled in a rhenium gasket for MS studies. This also served as an effective collimator for the 14.4 keV gamma rays. Liquid argon was used as a pressurizing medium [24,25]. A few ruby chips were included in the sample cavity for pressure measurements by way of the ruby $R1$ fluorescence pressure marker.

Powder XRD measurements were carried out at RT in angle-dispersive mode with a wavelength of $\lambda = 0.3738$ Å at the Pression Structure Imagerie par Contraste à Haute Énergie (PSICHÉ) beamline of Synchrotron SOLEIL (Paris). Pressurization was by means of a TAU piston-cylinder DAC with anvils having 200 μm diameter culets. The sample with a few ruby chips was loaded into a 100 μm diameter cavity drilled in a rhenium gasket preindented down to a final thickness of ~15 μm, and Ne was used as the pressure transmitting medium [25,26]. Diffraction images were collected using a MARS imaging plate detector and integrated using the FIT2D [27,28] and DIOPTAS software [29]. Powder diffraction patterns were analyzed using the GSAS-II software [30] to extract the unit-cell parameters.

The intensities of the diffraction peaks are affected by instrumental and sample problems (diamond x-ray absorption and low statistics in the random distribution of the sample crystallites). Therefore, the Rietveld refinement of the powder diffraction patterns did not result in a good enough fit. Hence, diffraction patterns were analyzed by using the whole profile fitting (Pawley) method [31]. The powder diffraction patterns consist of peaks mainly from the $FeCr_2O_4$ sample, as well as from the gasket (Re) and the pressure medium (Ne). These phases were considered in the refinements. The observed and refined curves are reported in Fig. S4 of the Supplemental Material [32]. The R_{wp} obtained in the refinement of each of the powder diffraction patterns is ~1%.

Resistance measurements in the TAU piston-cylinder DAC involved sample loaded into ~100 μm diameter cavities drilled in rhenium gaskets insulated with a layer of Al_2O_3-NaCl (3:1 wt%) mixed with epoxy. Conductive epoxy was used to connect exterior conducting Cu wires to microscopic triangular cut Pt foils. The latter served as electrodes in a dc four-probe configuration, leading from the pavilion of the anvil to near the center of the culet so as to overlap with the sample upon closure of the DAC. A few ruby fragments for pressure determination were located in the region between the Pt electrode tips overlapping the sample. No pressure transmitting medium was used, but pressure is effectively transmitted to the sample upon compression by way of the surrounding insulation. Pressure gradients are expected to be small in the distances (20–30 μm) between the tips of the Pt electrodes across which voltage measurements are made. For variable low temperature measurements, the DAC was placed on a probe connected to a "dip-stick" stepper-motor assembly, which by computer control slowly changed the height of the DAC above the cryogen level in a liquid nitrogen or helium Dewar. The temperature was monitored by a Lakeshore Si (DT-421-HR) diode in proximity to the DAC.

The calibration scales mentioned in Ref. [33] were used for pressure determination from the ruby fluorescence measurements. The error in the pressure determination is 5–10% of the reported average pressure from the ruby fluorescence measurements in the case of the MS and resistance experiments. In the case of the XRD measurements, pressure was determined from the ruby fluorescence spectra up to ~51 GPa. The Ne equation of state was used to ascertain pressures in the range 10–74 GPa [26]. Both methods give rather similar pressure values, with the difference not exceeding 0.5 GPa. The error in the pressure determination is about 2% of the reported average pressure.

III. RESULTS AND DISCUSSION

The evolution of the Fe Mössbauer spectra up to 93 GPa is summarized in the plots in Fig. 1, which show fitted spectra at RT (left panel) and at low temperatures (LTs; right panel), specifically the lowest cryogenic temperature for each specified pressure. We have fit each of these spectra with a

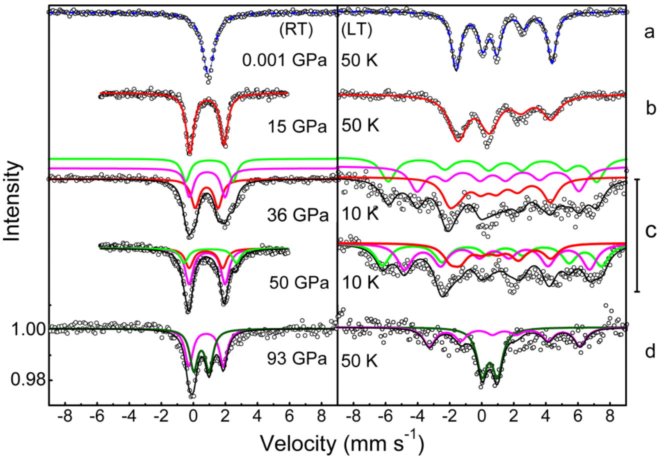

FIG. 1. Representative Fe Mössbauer spectra at RT (left panel) and LTs (right panel), in the four pressure regimes discussed in the text. Solid line through the data points represent the overall fit to the data from the sum of subcomponents shown. The subcomponents at 36 GPa have been displaced vertically for clarity. A similar suite has been fitted at 50 GPa with different abundances.

minimal number of spectral components, ensuring consistency between room and low temperature analyses. Figure 2 is a plot of the hyperfine interaction parameters derived from room and low temperature fits such as those exemplified in selected cases in Fig. 1. This delineates four pressure regimes that are now discussed in detail in the following subsections. In these regimes, the Mössbauer results are correlated to the pressure dependences of the resistance and the XRD structural data.

A. Ambient pressure to 10–12 GPa, cubic phase

The Mössbauer spectrum of FeCr$_2$O$_4$ at ambient pressure and RT showed sharp single line features emanating from Fe^{2+} in a cubic symmetry. Further spectra at low temperatures are similar to the temperature dependence shown in earlier work on this compound [3,9]. Temperature dependent XRD structural data in the literature [9,34] also indicate that a cubic-to-tetragonal transition is onset at $T_{\text{J-T}} \sim 135$ K. However, at $T > 135$ K, Mössbauer spectra already show deviations from cubic symmetry, as manifested in the temperature dependent QSs. This has been ascribed to a dynamical J-T effect operative at high temperatures. The tetragonal J-T distortions reorient dynamically among the three crystallographic axes on a time scale comparable to the inverse of the quadrupole precession frequency [10]. As such, a quadrupole interaction (and consequently QS) is discerned in the Mössbauer spectra. However, an average global cubic symmetry is discerned in the XRD structure. Below 135 K, a static J-T distortion occurs and is discerned as the near saturation QS ~ 2.7 mm s^{-1} in the Mössbauer spectra and tetragonality in the XRD pattern. At the lowest temperature, 5 K, the magnetic hyperfine splitting yields an internal magnetic field of $H_{hf} = 19.3$ T, consistent with previous investigations [3,19].

Upon compression, the Mössbauer spectra of the chromite at RT reveal a drastic change and apparent breaking of cubic symmetry, initiating as low as ~1 GPa; see middle panel of Fig. 2, where QS components evolve in the spectrum at RT.

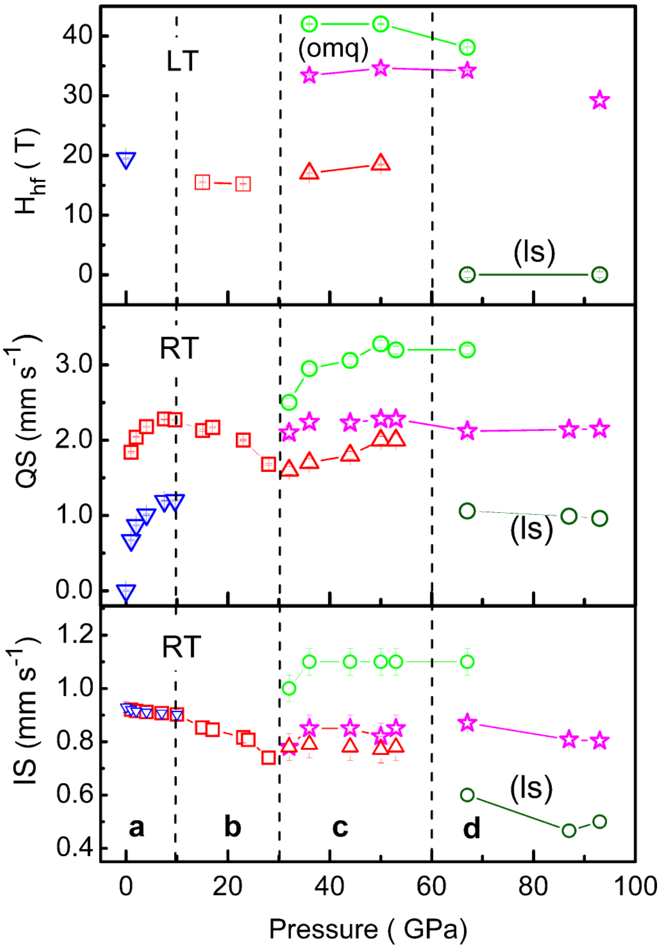

FIG. 2. Pressure dependences of the hyperfine interaction parameters from best fits to the Mössbauer spectra. Top panel has saturation magnetic hyperfine field H_{hf} values from the LT spectra. The QS and IS parameters from spectra at RT are in the middle and bottom panels. Four pressure regimes, designated (a)–(d) discussed in the text, are identified. Spectra in regime (a), where XRD discerns cubic behavior at 300 K, are best fit at this temperature with two QS components having similar IS values, as discussed in the text. Spectra in regime (b) are each fitted with a single component. Spectra in regime (c) are best fit with three subcomponents, two of which have a similar IS at 300 K. Large H_{hf} values associated with orbital moment quenching are delineated by the (omq) label. Spectra in regime (d) are each fitted with two subspectra at the highest pressures 87 and 93 GPa. The star (☆) and triangle (△) symbols refer to tetrahedral sites and the open circles (○) to octahedral sites from spinel inversion processes. Parameters for the low-spin sites are delineated by the (ls) labels.

The quadrupole split spectra in the pressure range of 2 to 10 GPa are each best fit with two subspectra with the same IS and different QS values. The abundance of the subspectra with a smaller QS decreases with increasing pressure. At ~10 GPa, the spectrum can be fitted with one QS component with a splitting of about 2.2 mm s^{-1}, which then shows a weak monotonic decrease upon further pressurization beyond 10 GPa. The IS decreases monotonically with increasing pressure (bottom panel of Fig. 2), as expected when there in an increase of s-electron density [35].

Interestingly, the XRD structural data at 300 K shows that the structure is definitively cubic up to ∼12 GPa. Therefore, how can the Mössbauer QS values in Fig. 2 (indicative of noncubic symmetry) be rationalized? We attribute this to the dynamical J-T effect alluded to earlier in the ambient pressure spectra [9]. The J-T distortion at high temperatures reorients among the three crystallographic axes with a frequency ω_R that is pressure dependent. Although we have chosen to fit these spectra with what appears to be two static QS components, these are likely dynamical spectral profiles reflecting the pressure dependent reorientation frequency of the J-T distortion among the crystallographic axes [36]. The MS spectral profile and fitted apparent QS values depend on how $1/\omega_R$ compares with the $1/\omega_Q$ quadrupole precession time window [9,10] (see Fig. S1 of the Supplemental Material [32]). The fact that there is more than one QS component at $P < 10$ GPa is an indication that the profiles are likely a bimodal distribution of QS and associated ω_R values, from varied local strains in the stressed sample. Note that MS is an atomic-scale probe that would be sensitive to spatially incoherent local distortions, even when XRD would register a globally averaged zero distortion and a cubic structure.

It is at slightly higher than this pressure regime, namely, at 11–15 GPa, that the XRD pattern starts to show definitive signatures of a tetragonal distortion at 300 K see (Figs. 3 and 4). This is consistent with the XRD pressure studies on a single crystal by Kyono *et al.* [20], who find a discontinuous volume change between 11.8 and 12.6 GPa. This has been considered to be a phase transition from a cubic (space group $Fd\bar{3}m$) to tetragonal structure (space group $I4_1/amd$), which is consistent with our XRD data.

We conclude that the XRD discerned cubic-to-tetragonal transition temperature $T_{\text{J-T}}$ associated with the static cooperative J-T effect and orbital ordering has risen dramatically from 135 K at ambient pressure to ∼300 K at $P \sim 12$ GPa. This static cooperative J-T distortion, and consequent tetragonality, is then manifested by both large QS values of static Mössbauer spectra (Fig. 1) and line broadening evolving to splittings in powder XRD profiles [see (220), (311), and (440) reflections] at 300 K and below [20].

The resistance at RT R(300 K) in Fig. 5 has a comparatively weak pressure dependence up to 10–12 GPa, after which there is a much stronger pressure dependence in the tetragonal phase discussed in the following section.

B. Tetragonal distortion, 12–30 GPa

Chromite now enters into the tetragonal-phase regime for $T \leqslant 300$ K. The tetragonal distortion progressively increases and is quite substantial by 30 GPa, as shown in the behavior of the pressure dependences of the c_T and $\sqrt{2}a_T$ lattice parameters in Fig. 4. The saturation magnetic Mössbauer spectra at low temperatures progressively start to lose fine-structure features, and by ∼24 GPa (shown in Fig. S3 of the Supplemental Material [32]), it is a rather smeared profile compared to the magnetic spectra at ambient and 15 GPa (Fig. 1, right-hand panel). Nevertheless, the extent of the magnetic hyperfine splitting is ∼15 T in this pressure regime. The pressure dependence of R(300 K), shown in Fig. 5, is substantially larger than that of the previous pressure regime, where a cubic phase is present. Mössbauer spectral profiles at 300 K are well represented by a single quadrupole doublet, where the QS values show a monotonic decrease (Figs. 1 and 2). The resistance temperature data can be well represented by activated hopping transport processes $R = R_0 \exp(E_a/(k_B T))$, where E_a is the activation energy. The charge gap for intrinsic conduction $E_g = 2E_a$ of this tetragonal phase is 500–300 meV in this pressure range, as deduced from fits to the linearized $R(T)$ data (see Fig. 5). The smearing of the magnetic spectrum at 24 GPa presumably prevails as pressure increases. A change in curvature of the monotonic pressure dependence of R(300 K) also initiates at ∼30 GPa (see Fig. 5). These are hints that an electronic transition is onset near to this pressure. Indeed, by 32 GPa, the Mössbauer spectrum at RT (shown in Fig. S3 of the Supplemental Material [32]), which is similar to the spectrum at 36 GPa in Fig. 1, develops broadened and structured features best fit with at least three QS components, to be discussed in the next section. Based on these behaviors, we delineate 30 GPa as the onset of a new electronic phase boundary. This does not involve a structural transition (see Figs. 3 and 4), and the tetragonal distortion, initiated earlier, continues to increase, as this phase boundary is traversed.

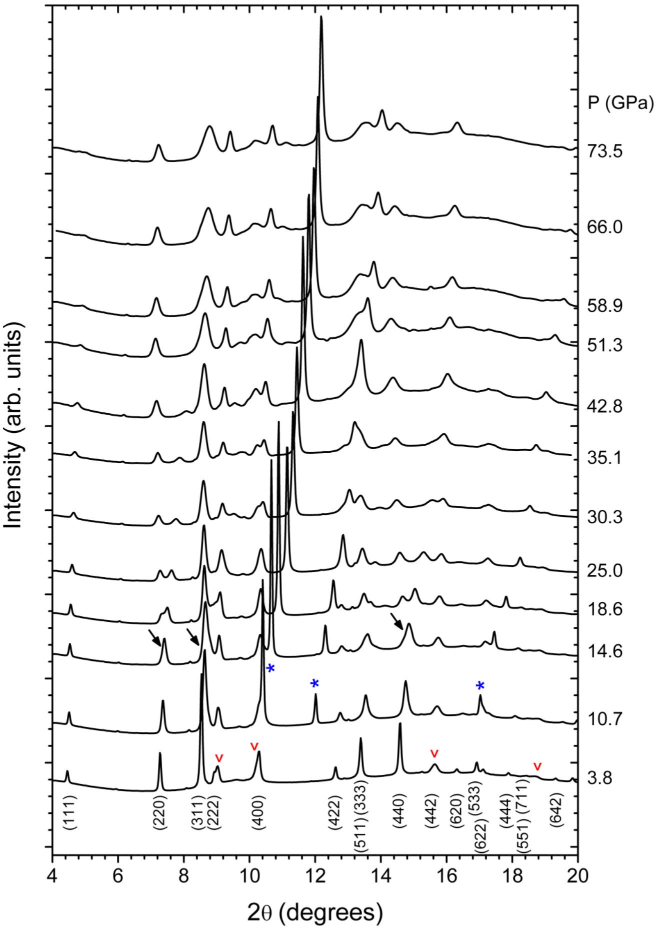

FIG. 3. Pressure evolution of the XRD patterns up to ∼74 GPa. Contamination reflections from the neon pressure transmitting medium (*) and the rhenium gasket (v) are indicated. The arrows indicate where tetragonal features become conspicuously manifested, peak broadenings evolving to splittings.

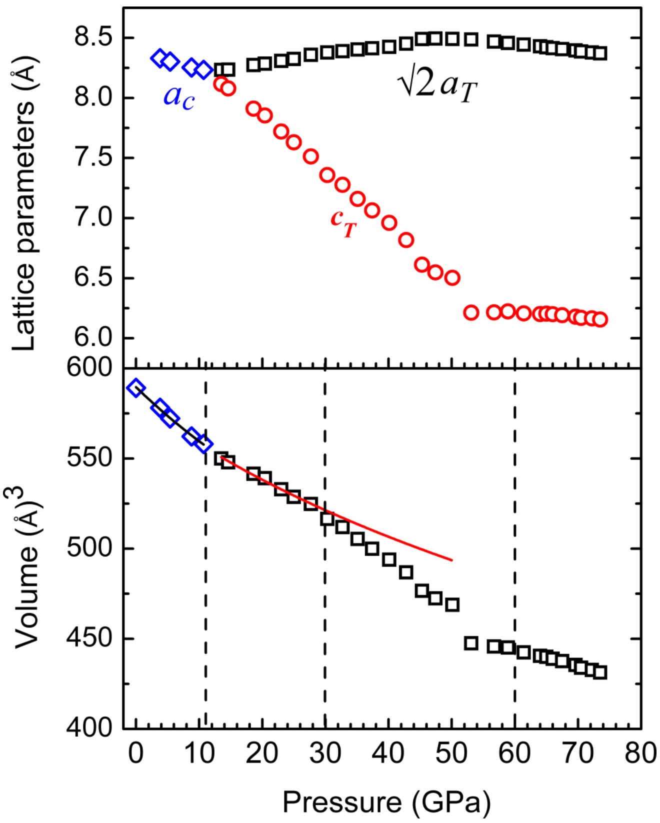

FIG. 4. Pressure dependences of the lattice parameters, cubic $\boldsymbol{a}_C$ values and both tetragonal c_T, as well as $\sqrt{2} \times \boldsymbol{a}_T$ values in the top panel. Unit-cell volume behavior is shown in the bottom panel. The discontinuous changes in c_T and unit-cell volume near 50 GPa should be noted. The vertical error bars do not exceed the size of the symbols in both panels. Solid lines through the data symbols in the lower panel are fits with a Birch-Murnaghan EOS [58]. For the cubic phase (ambient to 11 GPa), zero-pressure unit-cell volume $V_0 = 589.5(5)$ Å^3, bulk modulus $K_0 = 172(4)$ GPa, and its derivative fixed at $K_0' = 4$. The data point at ambient pressure used in the fit was taken from Kyono *et al.* [20]. In the range 12–30 GPa of the tetragonal phase $V_0 = 582(1)$ Å^3, $K_0 = 217(6)$ GPa, and $K_0' = 4$ (fixed). Note the significant deviation of the $V(P)$ data above 30 GPa from the obtained EOS. The vertical dashed lines demarcate the regimes identified in Figs. 1 and 2 (also see text).

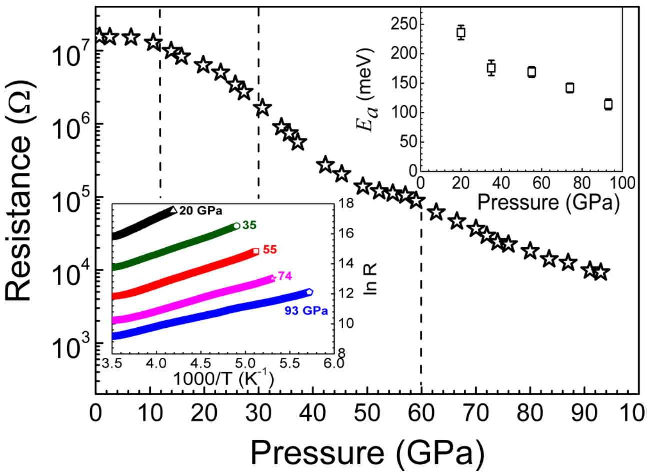

FIG. 5. Pressure dependence of the resistance at 300 K in the main panel. Bottom left inset shows linearized temperature dependent data at various pressures, assuming Arrhenius activated hopping transport, $\ln(R) \propto \frac{E_a}{k_B T} + \text{const}$. The activation energy E_a is obtained from the slope of fits to these plots, from whence the charge gap for intrinsic conduction $E_g = 2E_a$ is derived. Top right-hand inset shows the pressure dependence of E_a.

However, the pressure dependence of the unit-cell volume changes appreciably at compression beyond ∼30 GPa.

C. Orbital moment quenching and onset of site inversion, 30–60 GPa

Mössbauer spectra at RT in this range have a minimum of three subcomponents of varying abundances. This may be compared with the previous pressure regime, where a single QS component provided satisfactory fits. Lowering the temperature to 10 K also reveals complex magnetic spectra, substantially altered in comparison to the previous pressure regime, in that broadened components with much bigger H_{hf} values of ∼34 and 42 T are required, in addition to a component with H_{hf} of ∼20 T [see Fig. 1(c) regime]. The relative intensities of these components evolve to the extent that the 20 T subspectrum is a minority component by ∼60 GPa. This component is ascribed to remnant tetragonal phase from the preceding pressure regime. At 36 GPa, the large H_{hf} components of ∼33% abundance each represent sites whose orbital moment has quenched in this pressure regime.

This quenching has its origin in the following considerations; H_{hf} has two dominant contributions, from a Fermi contact term involving the net spin-up and spin-down s-electron density at the nucleus and a second contribution from the orbital moment [37,38]:

$$H_{hf} = +(\text{const.})\mu_B[\rho_s^{\uparrow}(0) - \rho_s^{\downarrow}(0)] \;-\; 2\mu_B\langle r^{-3}\rangle\langle l_Z\rangle, \quad (1)$$

where $\rho_S(0)$ is the spin density at the nucleus and l_Z is the z component of the orbital angular moment. These terms in Eq. (1) may be of opposite sign, and this normally accounts for the smaller H_{hf} values measured in ferrous compounds, well below the spin-only contribution from the first term, which is ∼44 T for Fe^{2+}. At sufficiently large tetragonal distortions and associated crystal-field (CF) values (see Fig. 6), the orbital term may be quenched. The l_Z contributions from the occupations in the 3d manifold average to zero, $\langle l_Z\rangle = 0$, and the Fermi contact term in Eq. (1) dictates the H_{hf} value [39,40].

In pressure regime (c), see Figs. 1(c) and 2(c), there are two such components. One is ascribed to tetrahedral sites, whose CF splitting has surpassed a critical value at ∼30 GPa from the increasing tetragonal distortion, such that orbital moment quenching occurs. The association of the H_{hf} ∼ 34 T component to tetrahedral sites is deduced from the QS ∼ 2 mm s^{-1} and IS ∼ 0.8 mm s^{-1} values at RT, similar (although the pressure dependences differ) to those in the preceding pressure regime (see Fig. 2). The orbital moment is apparently not fully quenched else a larger spin-only H_{hf} ∼ 44 T would be anticipated [37]. The third component exhibits this full quenching with H_{hf} ∼ 42 T and has substantially

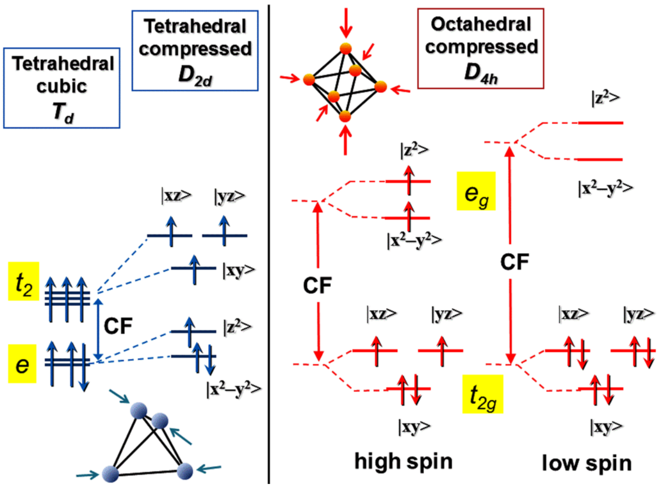

FIG. 6. Schematic of CF split 3*d* electronic level scheme for Fe^{2+} involving tetragonal distortions in tetrahedral and octahedral coordinations.

larger values of the IS $\sim 1.1\,\mathrm{mm\,s^{-1}}$ and QS increasing in the range $2.5-3.2\,\mathrm{mm\,s^{-1}}$ at 300 K in this pressure regime. This component is ascribed to progressive partial inversion of the tetragonal spinel and associated Fe $\leftrightarrow$ Cr site exchange, where high-spin Fe^{2+} enters octahedral sites, on the basis of comparatively high IS and especially high QS $\sim 3\,\mathrm{mm\,s^{-1}}$ values (which are atypical of Fe^{2+} in tetrahedral coordination for which QS $\sim 2\,\mathrm{mm\,s^{-1}}$ [41,42]). The increasing QS for this site in Fig. 2 points to an increasing distortion of the octahedral local environment. For most of this pressure regime, the Fe^{2+} at all sites is still high spin, and the XRD analysis indicates that the structure is still tetragonal in spite of the conspicuous electronic changes revealed by the evolved large H_{hf} components [top panel of Fig. 2(c)].

The high-spin Fe $\leftrightarrow$ Cr site exchange at high pressure is a somewhat interesting observation, given that at ambient conditions, $Cr^{3+}(d^3)$ has a strong preference for octahedral coordination because of the CF stabilization energy (CFSE; energy gain from electrons occupying lower lying t_{2g} orbitals) [43,44]. It has also been suggested in earlier work based on CF considerations that this is likely to be the case at high pressure geophysical conditions [45]. However, later work has shown that CFSE is not the sole determiner of cation distributions in spinels, as best delineated in Ref. [44]. Other important factors include configurational entropy associated with site disorder and the electronic entropy associated with electron occupancies in degenerate 3*d* energy levels [46]. Even ligand-metal *s* and *p* interactions control charge distributions and hence site preferences [47], and these could be appreciably altered at reduced interatomic spacings. To the best of our knowledge, these various contributions have not been investigated experimentally at very high pressure exceeding a few gigapascals.

In addition, *ab-initio* high pressure thermodynamics calculations to 20 GPa of the prototypical normal spinel $MgAl_2O_4$ have been used to calculate the degree of inversion versus temperature curves as a function of pressure [48]. These curves demonstrate that as pressure increases, the temperature window in which inversion rises rapidly tends to shift to lower temperatures, and inversion also develops a steeper dependence on temperature. These changes have a stronger than linear dependence on pressure. Following these trends and extrapolating to higher pressures, $P > 20$ GPa suggests that the onset of inversion could well commence at comparatively low temperatures of ~300 K at high enough pressures.

Other research on the lattice response of inversion has highlighted that normal spinels of the 2–3 type (involving divalent and trivalent cations) tend to become more inverse with increasing pressure, because the inverse distribution generally has a smaller volume than the normal counterpart [49]. Moreover, available evidence indicates that the bulk modulus of normal spinels exceed that of the inverse variant [50].

Note that the pressure dependence of the unit-cell volume in Fig. 4 changes appreciably to a steeper decrease of unit-cell volume as pressure rises above 30 GPa. This leads to a clear deviation of the $V(P)$ dependence from the equation of state (EOS) calculated in the range 12–30 GPa. We interpret this as the lattice response to evolving inversion processes, mentioned in the foregoing paragraph.

In addition, the hyperfine interaction parameters (QS and IS) derived from fitting the Mössbauer spectra at RT [see Fig. 2(c)] exceed typical values for Fe^{2+} in fourfold coordination and are closely compatible with those for sixfold (octahedral) coordination [41,42].

We contend that both the lattice and electronic responses of above, evidences the evolving (Fe $\leftrightarrow$ Cr) site inversion, which is triggered somewhere in the range 25–30 GPa at 300 K. The driving force for this is likely a combination of factors mentioned in the forgoing few paragraphs. High-spin Fe^{2+} at these high densities (and comparatively low temperatures of 300 K) has developed higher octahedral site preference energetics compared with Cr^{3+}. This is in addition to a compacted polyhedral volume involving tetrahedral coordination at these high densities and its anticipated inability to accommodate high-spin Fe^{2+} with its comparatively large ionic radius [51].

Towards the higher end of this pressure regime, at 50–55 GPa, there is a discontinuous decrease in both *c* lattice parameter and unit-cell volume, and the pressure dependences of the c_T and $\sqrt{2}a_T$ parameters alter substantially (Fig. 4). The pressure dependence of the unit-cell volume also alters to become much weaker, as pressure rises above where the discontinuity has occurred.

Mössbauer spectra (see Figs. S2 and S3 of the Supplemental Material [32]) at both RT and 50 K at the next highest pressure of 67 GPa show significant changes to those taken in the 30–60 GPa regime. Note that the pressure dependence of R(300 K) shows an inflection in the range 55–60 GPa. Therefore, ~60 GPa is delineated as another phase transition boundary almost coinciding with the changes seen in the pressure dependence of the lattice response described above. By way of further information, an Arrhenius fit applicable to the *R(T)* data over an extended temperature range yields a charge gap of $E_g \sim 340$ meV at ~55 GPa.

D. Onset of spin crossover, 60–93 GPa

The Mössbauer spectrum at 67 GPa and RT (see Supplemental Material [32], Fig. S2) shows the emergence of a component with a smaller QS $\sim 1\,\text{mm}\,\text{s}^{-1}$ than seen in any of the two previous pressure regimes (Figs. 1 and 2). Lowering the temperature to 50 K shows that this QS component persists against a background where there is a coexisting subspectrum having $H_{hf} \sim 35\,\text{T}$. The RT spectrum at 87 GPa may be fitted with only two components, one with a small QS $\sim 1\,\text{mm}\,\text{s}^{-1}$(IS $= 0.45\,\text{mm}\,\text{s}^{-1}$) and the other having QS $\sim 2\,\text{mm}\,\text{s}^{-1}$(IS $= 0.85\,\text{mm}\,\text{s}^{-1}$). There is a similar spectral profile and deconvolution at 93 GPa, where additionally a spectrum was measured at 50 K (Fig. 1, right-hand panel). The small QS component persists as a doublet down to these temperatures. Whereas the large QS component exhibits magnetic hyperfine structure with $H_{hf} \sim 30\,\text{T}$. This behavior and values of the hyperfine interaction parameters suggest that the small QS component represents low-spin Fe^{2+} sites [41,52]. Such low-spin Fe^{2+} must be in sites other than tetrahedral locations, where the low-spin configuration does not arise, due to the much smaller CF splitting compared with octahedral coordination [44,53]. The low-spin Fe^{2+} must, therefore, be in octahedral sites, which have arisen from Fe ↔ Cr partial inversion processes and correspond to Fe^{2+} with atomic spin $S = 0$ and $3d$ orbital population ${t_{2g}}^6{e_g}^0$ with electron spin depiction $(\uparrow\downarrow\uparrow\downarrow\uparrow\downarrow)()$. The rest of the tetrahedral iron sites are still high spin.

This spin pairing at selected (octahedral) sites occurs when the CF splitting is such (see Fig. 6) that the cost of occupying the higher lying e_g states and maximizing the configuration of parallel spins exceeds the cost of rather pairing electrons $(\uparrow\downarrow)$ in lower lying t_{2g} orbitals (breakdown of Hund's rule). The latter spin-pairing cost is the *intra-atomic* ferromagnetic exchange energy $J \sim 1\,\text{eV}$ [52,54]. The symmetric distribution of electrons in the t_{2g} orbitals (see Fig. 6, low-spin state) renders the small quadrupole interaction and consequently a relatively small QS $\sim 1\,\text{mm}\,\text{s}^{-1}$, compared to the typical high-spin values of QS $\sim 2\,\text{mm}\,\text{s}^{-1}$ in ferrous compounds [52].

Note that low-spin Fe^{2+} has a similar ionic radius to that of Cr^{3+}($\sim$0.61 Å). Moreover, the CFSE for $Fe^{2+}({t_{2g}}^6{e_g}^0)$ in octahedral coordination far exceeds that of $Cr^{3+}({t_{2g}}^3{e_g}^0)$ [43,44]. Hence, if CFSE aspects alone are considered, the energy gain of having low-spin Fe^{2+} in octahedral coordination exceeds the cost of Cr^{3+} populating tetrahedral sites in the posited Fe ↔ Cr inversion process.

This spin crossover is also consistent with the discontinuities seen in the lattice parameters and unit-cell volume in the 50–60 GPa regime in Fig. 4 [51], as well as the upward inflection in R(300 K) behavior at 55–60 GPa in Fig. 5 [55]. This is, then, supposed to be the pressure regime where spin crossover is triggered. Differences in this spin crossover onset pressure identified by the three techniques is ascribed to the different pressure transmitting media and degrees of hydrostaticity in the DAC (see Experimental section).

In this very high pressure phase, stable beyond $\sim$90 GPa, about half the Fe^{2+} sites are low spin, and the rest remain high spin [see Fig. 1(d) regime]. Even in the absence of XRD data beyond 74 GPa, we suggest this is due to evolved spinel inversion processes [already initiated in the preceding pressure regime, Fig. 1(c) at $\sim$30 GPa], rather than a structural change to a postspinel phase in which cations occur in octahedral coordination where low-spin states could ensue [15,44,56]. Such a drastic structural change from tetragonal to postspinel would likely have resulted in a discontinuous change or signature change in slope of the R(300 K) data in Fig. 5. Instead, this is smoothly varying in this pressure regime up to a highest pressure of 93 GPa.

In addition, note that the temperature dependent resistance data has a persistent negative temperature coefficient dR/dT and activated semiconducting behavior up to the highest pressure. The R(300 K) value decreases by only three orders of magnitude over the full pressure range to near 100 GPa. The charge gap at 93 GPa is $E_g \sim 200\,\text{meV}$ from an Arrhenius fit, which is applicable over the entire temperature range 300–10 K (see Fig. 5). Evidently, this mixed high-spin/low-spin lattice configuration remains nonmetallic to megabar pressures.

IV. CONCLUSIONS

Ferrous chromite to nearly a megabar represents an exemplary case of the pressure tuned interplay of lattice, orbital, and spin degrees of freedom associated with coexisting tetrahedral and octahedral $3d$ electronic manifolds in spinels, summarized as follows:

(i) The cubic-to-tetragonal transition occurs at RT at $\sim$12 GPa. It has increased from $T_{\text{J-T}} \sim 135\,\text{K}$ at ambient pressure to 300 K at $\sim$12 GPa. Thus, ferrous chromite is likely to be orbitally ordered at RT in this pressure regime near $\sim$12 GPa.

(ii) Orbital moment quenching is realized in the system by $\sim$30 GPa, beyond which large internal magnetic hyperfine fields H_{hf} of 34–42 T occur in the Mössbauer spectral profile. In the range 30–60 GPa, the hyperfine interaction parameters of the components suggests an assignment of tetrahedral sites both with and without orbitally quenched moments (H_{hf} values of $\sim$34 T and $\sim$20 T, respectively), as well as an additional component ascribed to Fe ↔ Cr (tetrahedral ↔ octahedral) site inversion ($H_{hf} \sim 42\,\text{T}$). This electronic change and cation exchange has an associated lattice response involving a steeper change in unit-cell volume as pressure rises beyond $\sim$30 GPa.

(iii) In the vicinity of $\sim$60 GPa, spin crossover is triggered and identified by a discontinuous decrease in unit-cell volume and drastic decrease in its pressure dependence upon further compression. The Mössbauer spectra above 60 GPa develop a diamagnetic doublet with hyperfine interaction parameters typical of a low-spin state (comparatively small QS and IS values). Such octahedral site occupation attains an abundance of $\sim$50% at 93 GPa in coexistence with tetrahedral sites in the high-spin state.

(iv) Up to 74 GPa, the XRD data shows a progressively distorted structure with tetragonal space group $I4_1/amd$. The reduced tetrahedral volume, as well as (configurational and electronic) entropic considerations at high pressure, trigger the Fe ↔ Cr site inversion in the vicinity of $\sim$30 GPa. The high temperature window in which site inversion becomes appreciable in spinels at ambient pressure has shifted drastically downwards to encompass 300 K in this iron chromite at high pressure. At higher densities in the vicinity of $\sim$60 GPa, the high-spin Fe^{2+} ionic volume cannot be accommodated in the compressed octahedral interior as well. This also contributes to triggering a change to a low-spin configuration with a smaller cationic radius that may be located within compacted octahedral interiors.

(v) The very high pressure phase beyond the limits of the XRD data at ~74 GPa is considered to have further evolved cationic (tetrahedral ↔ octahedral) exchange such that the low-spin configuration is stabilized at about half the Fe sites. The resistance data shows no further anomalies up to the highest pressure of ~93 GPa. Therefore, a structural transition to a postspinel structure, which could also provide the requisite octahedral haven for low-spin Fe, is considered unlikely.

Finally, note that the XRD data indicates quite a substantial 30% reduction in unit-cell volume over the full pressure range. We would have anticipated that the corresponding bandwidth broadening from polyhedral distortions would lead to an appreciable reduction in or collapse of the charge gap. However, the gap does not show this appreciable change over the extended pressure range.

This is attributable to the behavior of the effective on-site repulsion parameter (U_{eff} determining the gap between upper and lower Hubbard bands), which renders the nonmetallic (Mott insulator type) behavior to these partially filled 3*d* band oxides. The U_{eff} in high-spin d^6(Fe^{2+}) and d^3(Cr^{3+}) electronic configurations is constant or increases, respectively, with increasing pressure [54,57]. Spin crossover further contributes to increasing U_{eff} in d^6 systems.

Evidently, these increases in U_{eff} due to positive dependences on the CF splitting, compensate the band-broadening induced reduction of the charge gap in this mixed low-spin/high-spin lattice configuration of the very high pressure phase of $\mathrm{FeCr_2O_4}$. This would manifest as persistent charge carrier localization, conducive to the tetragonal J-T phase stabilization over such a wide pressure range.

At ~93 GPa, the system remains nonmetallic with a charge gap of ~200 meV. Ferrous chromite near a megabar is a partially inverted tetragonal spinel $[\mathrm{Fe}_{1-x}\mathrm{Cr}_x]\{\mathrm{Fe}_x\mathrm{Cr}_{2-x}\}\mathrm{O}_4$ ($x \sim 0.5$), which has persistent "Mottness" (strongly correlated electron behavior), involving mixed spin-states in tetrahedral and octahedral sites.

ACKNOWLEDGMENTS

This research was supported by the Israel Science Foundation (Grant No. 1489/14). G.R.H. acknowledges financial support from the National Research Foundation of South Africa (Grant No. 87808).

---

[1] G. Shirane, D. E. Cox, and S. J. Pickart, J. Appl. Phys. **35**, 954 (1964).

[2] K. Tomiyasu, H. Hiraka, K. Ohoyama, and K. Yamada, J. Phys. Soc. Jpn. **77**, 124703 (2008).

[3] S. Nakamura and A. Fuwa, Phys. Procedia **75**, 747 (2015).

[4] S. Bordács, D. Varjas, I. Kézsmárki, G. Mihály, L. Baldassarre, A. Abouelsayed, C. A. Kuntscher, K. Ohgushi, and Y. Tokura, Phys. Rev. Lett. **103**, 077205 (2009).

[5] K. Singh, A. Maignan, C. Simon, and C. Martin, App. Phys. Lett. **99**, 172903 (2011).

[6] A. Maignan, C. Martin, K. Singh, Ch. Simon, O. I. Lebedev, and S. Turner, J. Solid State Chem. **195**, 41 (2012).

[7] J. van-den-Brink and D. I. Khomskii, J. Phys.: Condens. Matter **20**, 434217 (2008).

[8] K. Tsuda, D. Morikawa, Y. Watanabe, S. Ohtani, and T. Arima, Phys. Rev. B **81**, 180102 (2010).

[9] M. Tanaka, T. Tokoro, and Y. Aiyama, J. Phys. Soc. Jpn. **21**, 262 (1966).

[10] Quadrupole precession frequency $\omega_Q = (\frac{1}{2}\,\mathrm{e}V_{zz}Q)/\hbar$, where V_{zz} is the maximum value of the electric field gradient and Q the quadrupole moment. The numerator is the quadrupole (spectral doublet) splitting QS in the static limit. The quadrupole precession frequency is $\omega_Q \sim 14 \times 10^7\ \mathrm{rad\,s^{-1}}$ for QS $\sim 2\ \mathrm{mm\,s^{-1}}$.

[11] S. H. Shim, T. S. Duffy, and G. Y. Shen, Nature (London) **411**, 571 (2001).

[12] W. R. Peltier and L. P. Solheim, Geophys. Res. Lett. **19**, 321 (1992).

[13] D. Errandonea, in *Pressure-Induced Phase Transitions in AB_2X_4 Chalcogenide Compounds*, edited by F. J. Manjón, I. Tiginyanu, and V. Ursaki (Springer-Verlag, Berlin, 2014), Vol. 189, pp. 53–73

[14] D. Errandonea, R. S. Kumar, F. J. Manjón, V. V. Ursaki, and E. V. Rusu, Phys. Rev. B **79**, 024103 (2009).

[15] T. Yamanaka, A. Uchida, and Y. Nakamoto, Am. Mineral. **93**, 1874 (2008).

[16] M. Chen, J. Shu, H. K. Mao, X. Xie, and R. J. Hemley, Proc. Natl. Acad. Sci. USA **100**, 14651 (2003).

[17] F. D. Saccone, S. Ferrari, D. Errandonea, F. Grinblat, V. Bilovol, and S. Agouram, J. Appl. Phys. **118**, 075903 (2015).

[18] S. Ferrari, R. S. Kumar, F. Grinblat, J. C. Aphesteguy, F. D. Saccone, and D. Errandonea, Solid State Sci. **56**, 68 (2016).

[19] F. Hartmann-Boutron and P. Imbert, J. Appl. Phys. **39**, 775 (1968).

[20] A. Kyono, S. A. Gramsch, T. Yamanaka, D. Ikuta, M. Ahart, B. O. Mysen, H. K. Mao, and R. J. Hemley, Phys. Chem. Miner. **39**, 131 (2012).

[21] G. R. Hearne, M. P. Pasternak, and R. D. Taylor, Rev. Sci. Instrum. **65**, 3787 (1994).

[22] The hyperfine interaction parameters, including Fe site abundances, are derived from fitting the spectral envelope with Lorentzian subcomponents. The isomer (chemical) shift IS is proportional to the *s*-electron density at the Fe nucleus and is influenced by *d*-electron shielding. The quadrupole doublet-splitting or line shift, QS, is proportional to the deviation from cubic symmetry of both the surrounding electron configuration and nearest neighbor atoms. The IS, QS, and H_{hf} (from magnetically split hyperfine structure) parameters have distinct "fingerprint" values for both valences and spin states of Fe^{2+} ($3d^6$) and Fe^{3+}($3d^5$). In complex spectra, with appreciable overlap of subcomponents, mainly IS and to a lesser extent H_{hf} values of fitted subspectra, are obtained with good reliability, to establish the electronic state of the Fe.

[23] G. Y. Machavariani, M. P. Pasternak, G. R. Hearne, and G. K. Rozenberg, Rev. Sci. Instrum. **69**, 1423 (1998).

[24] D. Errandonea, R. Boehler, S. Japel, M. Mezouar, and L. R. Benedetti, Phys. Rev. B **73**, 092106 (2006).

[25] S. Klotz, J. C. Chervin, P. Munsch, and G. L. Marchand, J. Phys. D **42**, 075413 (2009).

[26] A. Dewaele, F. Datchi, P. Loubeyre, and M. Mezouar, Phys. Rev. B **77**, 094106 (2008).

[27] A. P. Hammersley, S. O. Svensson, M. Hanfland, A. N. Fitch, and D. Hausermann, High Pressure Res. **14**, 235 (1996).

[28] A. P. Hammersley, European Synchrotron Radiation Facility (ESRF) Internal Report No. ESRF97HA02T (1997).

[29] C. Prescher and V. B. Prakapenka, High Pressure Res. **35**, 223 (2015).

[30] B. H. Toby and R. B. Von-Dreele, J. Appl. Crystallogr. **46**, 544 (2013).

[31] G. S. Pawley, J. Appl. Crystallogr. **14**, 357 (1981).

[32] See Supplemental Material at http://link.aps.org/supplemental/10.1103/PhysRevB.95.045110 for further plots of selected Mössbauer spectra and fitted XRD patterns.

[33] A. D. Chijioke, W. J. Nellis, A. Soldatov, and I. F. Silvera, J. Appl. Phys. **98**, 114905 (2005).

[34] S. Ohtani, Y. Watanabe, M. Saito, N. Abe, K. Taniguchi, H. Sagayama, T. Arima, M. Watanabe, and Y. Noda, J. Phys.: Condens. Matter **22**, 176003 (2010).

[35] The IS has the formulation IS $= -(\text{constant})\rho_s(0) + (\text{constant}')$, where the constants are atomic and nuclear parameters. In this formulation, $\rho_s(0)$ is the s-electron density at the nucleus. This indicates that IS decreases, as the s-electron density increases under compression.

[36] J. A. Tjon and M. Blume, Phys. Rev. **165**, 456 (1968).

[37] The magnetic hyperfine field is a result of the nuclear Zeeman splitting of ^{57}Fe nuclear levels due to an internal magnetic field at the nucleus. The primary contribution to this internal field H_{hf} is from the contact term. This is the effect of d-electron spin polarization on the s-electrons. Other contributions to H_{hf} are from comparatively small dipolar and orbital terms. In high-spin ferric iron, the orbital and dipolar terms are negligibly small. The orbital term in high-spin ferrous iron and low-spin ferric iron may be appreciable and of opposite sign to the contact term. At well below the magnetic ordering temperatures, H_{hf} in high-spin ferric oxides is typically clustered around ~50 T, whereas in ferrous compounds, it may range from near zero to 44 T, depending on the orbital configuration.

[38] N. N. Greenwood and T. C. Gibb, *Mössbauer Spectroscopy* (Chapman and Hall, London, 1971).

[39] J. Kuneš, H. Rosner, D. Kasinathan, C. O. Rodriguez, and W. E. Pickett, Phys. Rev. B **68**, 115101 (2003).

[40] W. M. Xu and M. P. Pasternak, Hyperfine Interact. **144**, 175 (2002).

[41] R. E. Vandenberghe and E. D. Grave, in *Mössbauer Spectroscopy (Tutorial Book)*, edited by Y. Yoshida and G. Langouche (Springer-Verlag, Berlin, 2013), pp. 91–184.

[42] M. D. Dyar, D. G. Agresti, M. W. Schaefer, C. A. Grant, and E. C. Sklute, Annu. Rev. Earth Planet. Sci. **34**, 83 (2006).

[43] The CFSE, is the energy gained in populating low lying orbitals of the 3d CF split levels. For example, if the splitting between e_g and t_{2g} levels is denoted CF in octahedral coordination, then each electron in a t_{2g} orbital stabilizes the cation by $2/5$(CF) and each electron in the higher lying e_g orbitals detabilizes it by $3/5$(CF); see also Fig. 6.

[44] R. G. Burns, *Mineralogical Applications of Crystal Field Theory* (Cambridge University Press, Cambridge, UK, 1993).

[45] R. G. Burns, Geochim. Cosmochim. Acta **39**, 857 (1975).

[46] H. St. C. O'Neil and A. Navrotsky, Am. Mineral. **68**, 181 (1983).

[47] J. K. Burdett, G. D. Price, and S. L. Price, J. Am. Chem. Soc. **104**, 92 (1982).

[48] S. Da Rocha and P. Thibaudeau, J. Phys.: Condens. Matter **15**, 7103 (2003).

[49] R. M. Hazen and A. Navrotsky, Am. Mineral. **81**, 1021 (1996).

[50] R. M. Hazen and H. Yang, Am. Mineral. **84**, 1956 (1999).

[51] According to R. D. Shannon, Acta Crystallogr., Sec. A **32**, 751 (1976), the ionic radii at ambient conditions of Fe^{2+} in sixfold coordination in high-spin and low-spin states are 0.78 and 0.61 Å, respectively. Cr^{3+} in sixfold coordination has an ionic radius of 0.615 Å.

[52] P. Gütlich, E. Bill, and A. X. Trautwein, *Mössbauer Spectroscopy and Transition Metal Chemistry: Fundamentals and Applications* (Springer, Berlin, 2011).

[53] The crystal field splitting (CF) for tetrahedral coordination is ~4/9 of that for octahedral coordination, involving the same cation-anion distances.

[54] S. G. Ovchinnikov, J. Exp. Theor. Phys. **107**, 140 (2008).

[55] This inflection signature would likely have been more pronounced if a higher degree of hydrostaticity could be obtained, in the case where an effective pressure transmitting medium was used to such high pressure. This would require prohibitively difficult spot welding (direct contact) to the microscopic sample from the outset, prior to loading into the minute cavity. The effect of poor hydrostaticity is normally to smear our transition points, as well as to shift transition pressures.

[56] In the postspinel phase, about half the cations occur in octahedral coordination sites where low-spin states could ensue. The rest of the sites are of higher coordination number (at least eightfold), where the low-spin Fe configuration is not energetically favored in the 3d CF splitting setting.

[57] I. S. Lyubutin, S. G. Ovchinnikov, A. G. Gavriliuk, and V. V. Struzhkin, Phys. Rev. B **79**, 085125 (2009).

[58] F. Birch, J. Geophys. Res. **83**, 1257 (1978).